Insight into petrophysical properties of deformed sandstone reservoirs

Anita Torabi, Haakon Fossen, and Alvar Braathen

ABSTRACT

We use samples from undeformed and deformed sandstones (single deformation band, deformation band cluster, slip-surface cataclasite, and fault core slip zone) to characterize their petrophysical properties (porosity, permeability, and capillary pressure). Relationships between permeability and porosity are described by power-law regressions where the power-law exponent (D) decreases with the increasing degree of deformation (strain) experienced by the sample from host rock (D, ~9) to fault core (D, ~5). The approaches introduced in this work will allow geologists to use permeability and/or porosity measurements to estimate the capillary pressures and sealing capacity of different fault-related rocks without requiring direct laboratory measurements of capillary pressure. Results show that fault core slip zones have the highest theoretical sealing capacity (>140-m [459-ft] oil column in extreme cases), although our calculations suggest that deformation bands can locally act as efficiently as fault core slip zones in sealing nonwetting fluids (in this study, oil and CO_2). Higher interfacial tension between brine and CO_2 (because of the sensitivity of CO_2 to temperature and pressure) results in higher capillary pressure and sealing capacity in a brine and CO_2 system than a brine and oil system for the same samples.

INTRODUCTION

The petrophysical properties of highly porous sandstone reservoirs undergo significant changes as a result of deformation. Knowledge of the petrophysical properties of deformed sandstone and its undeformed host rock is essential for predicting

Manuscript received March 6, 2012; provisional acceptance May 10, 2012; revised manuscript received August 30, 2012; final acceptance October 3, 2012.
DOI:10.1306/10031212040

AUTHORS

ANITA TORABI ~ *Centre for Integrated Petroleum Research (Uni CIPR), Uni Research, Allegt. 41, N-5007 Bergen, Norway; anita.torabi@uni.no*

Anita Torabi is a senior researcher and a project leader at the Centre for Integrated Petroleum Research (Uni CIPR), Uni Research. She holds a Ph.D. in petroleum structural geology from the University of Bergen, Norway (2007). Her main research activities include the mechanism and mechanics of faulting, fault-related folding, and fluid flow in deformed reservoirs; CO_2 storage underground; and diagenesis in fault zone.

HAAKON FOSSEN ~ *Department of Earth Science, University of Bergen, Bergen, Norway; haakon.fossen@geo.uib.no*

Haakon Fossen joined the University of Bergen after several years as a structural geologist within exploration and production departments in Statoil. His current research interests include deformation of sandstones, rifting, and continental collisions. He holds a C.Sc. degree from the University of Bergen (1986) and a Ph.D. from the University of Minnesota (1992).

ALVAR BRAATHEN ~ *University Centre in Svalbard, Longyearbyen, Norway; alvar.braathen@unis.no*

Alvar Braathen works as a structural geologist for the University Centre in Svalbard, following years at the Centre for Integrated Petroleum Research, University of Bergen, and the Geological Survey of Norway. His current research covers sedimentary basin development, with a focus on fault and fracture characteristics. He holds C.Sc. (1991) and D.Sc. (1994) degrees from the University of Tromsø, Norway.

ACKNOWLEDGEMENTS

This study has been partly funded through Consortium R&D Project 429 207806/E20 (IMPACT Project) and partly through the Fault Facies Project. We thank the sponsors of these projects, the Research Council of Norway (CLIMIT and Petromaks programs), Statoil, and ConocoPhilips. We also thank AAPG Editor Stephen E. Laubach and the four reviewers John G. Solum, Andrew R. Thomas, Mark Andersen, and an anonymous reviewer for the constructive

comments. We thank Stephen Eaton for reviewing and copyediting the final version of the manuscript.
The AAPG Editor thanks the following reviewers for their work on this paper: Mark Andersen, John G. Solum, and an anonymous reviewer.

EDITOR'S NOTE

Color versions of Figures 1 and 11 may be seen in the online version of this article.

fluid flow through such reservoirs. Faults are heterogeneous structures whose geologic and petrophysical properties may show abrupt lateral variations that can make faults act as barriers, baffles, or conduits to fluid flow (Smith, 1966; Gibson, 1994; Fisher and Knipe, 2001; Torabi and Fossen, 2009). Faults can control fluid flow by juxtaposing reservoir rocks against nonreservoir rocks or by making barriers to fluid flow through seals or fault rocks (Fisher and Knipe, 2001). This may reduce production rates in a petroleum reservoir and, in case of CO_2 storage, may affect the injection rate and the total capacity of the reservoir. Consequently, faults may have considerable effects on hydrocarbon field production and CO_2 storage management alike. One of the objectives of this article is to explore the petrophysical characteristics (e.g., porosity, permeability, and capillary pressure) of fault-related rocks found in porous sandstones, using different methods for estimation of these properties, such as in-situ, laboratory, and image-processed–based (Torabi et al., 2008) methods. These results are used in analyzing statistical and empirical relationships between the petrophysical properties.

A common approach to fault seal analysis is to use simple algorithms for seal capacity by clay smear, as reviewed by Yielding et al. (1997). An alternate approach, which will be used in this study, considers faults (and stratigraphic seals) as tabular zones whose sealing capacity is controlled by fault-intrinsic properties such as porosity and permeability. This approach offers a possible assessment of capillary seal where the sealing capacity of the zone or layer relies on the size of pore throats and capillary forces between wetting and nonwetting phases. The capillary seal model allows for partially sealing faults, where the sealing capacity is governed by a critical pressure difference across the fault induced by the capillary forces, that is, an equilibrium situation acquired over geologic time in petroleum reservoirs that may be altered during production or injection (Fisher et al., 2001; Jolley et al., 2007). When the critical pressure is overcome for the liquid or vapor in question, flow is controlled by the relative permeability of fluids (e.g., Manzocchi et al., 2010).

The fluid-flow behavior of faults in a petroleum reservoir is a function of their capillary entry pressure, porosity, permeability, and spatial continuity (e.g., Gibson, 1994; Knipe, 1997). The permeability of a fault zone is a function of its architecture (e.g., fault zone components and their geometry) and the flow properties of fault-related rocks and fractures (Caine et al., 1996; Fisher and Knipe, 1998; Gibson, 1998; Wibberley et al., 2008; Braathen et al., 2009). Major faults are generally surrounded by an enveloping volume of structures

of different scales exhibiting smaller faults, deformation bands, and fractures, defined by most authors as the damage zone (Figure 1A; e.g., Chester and Logan, 1986; Peacock et al., 2000; Schultz and Fossen, 2008; Braathen et al., 2009; Torabi and Berg, 2011). Damage zones in highly porous sandstones tend to be dominated by deformation bands (Fossen et al., 2007). Deformation bands can be classified into different types based on deformation mechanisms (Fossen et al., 2007), and cataclastic bands, that is, bands involving significant grain crushing, generally have a higher impact on the petrophysical properties (e.g., porosity, permeability, and capillary pressure) of the damage zone than noncataclastic bands. Damage zones are believed to form during fault-tip propagation and grow during continued slip accumulation on the main fault surface of the fault core (Shipton and Cowie, 2003). Most of the displacement is accommodated within the fault core, which, in nearly all cases, is found to be substantially thinner than the damage zone. Previous workers have provided some data on the petrophysical properties of faults (e.g., Antonellini and Aydin, 1994; Fisher and Knipe, 1998, 2001; Gibson, 1998; Sternlof et al., 2004), their sealing capacity (e.g., Gibson, 1994; Yielding et al., 1997; Fisher and Knipe, 2001; Færseth, 2006), and the distribution of fault rock types (e.g., Knipe, 1997; Childs et al., 2007). As outlined in Braathen et al. (2009), fault cores in sandstone are made up of several elements such as membranes (fault-parallel layers) of fault rocks (fault gouge), host and fault-rock lenses, slip surface(s) bounding significantly crushed sandstone (slip-surface cataclasites), fractures, and deformation bands (Figure 1). The slip surface with its deformed walls have been termed "slip zones" (Foxford et al., 1996), whereas the crushed slip-surface wall rocks in porous sandstone have been labeled slip-surface cataclasites (Tueckmantel et al., 2010). Their appearance is similar to cataclastic deformation bands, but the porosity and, especially, the permeability tend to be lower for slip-surface cataclasites (Tueckmantel et al., 2010).

The internal distribution of fault core elements remains poorly understood, limiting predictions around fault core architecture. Therefore, knowl-

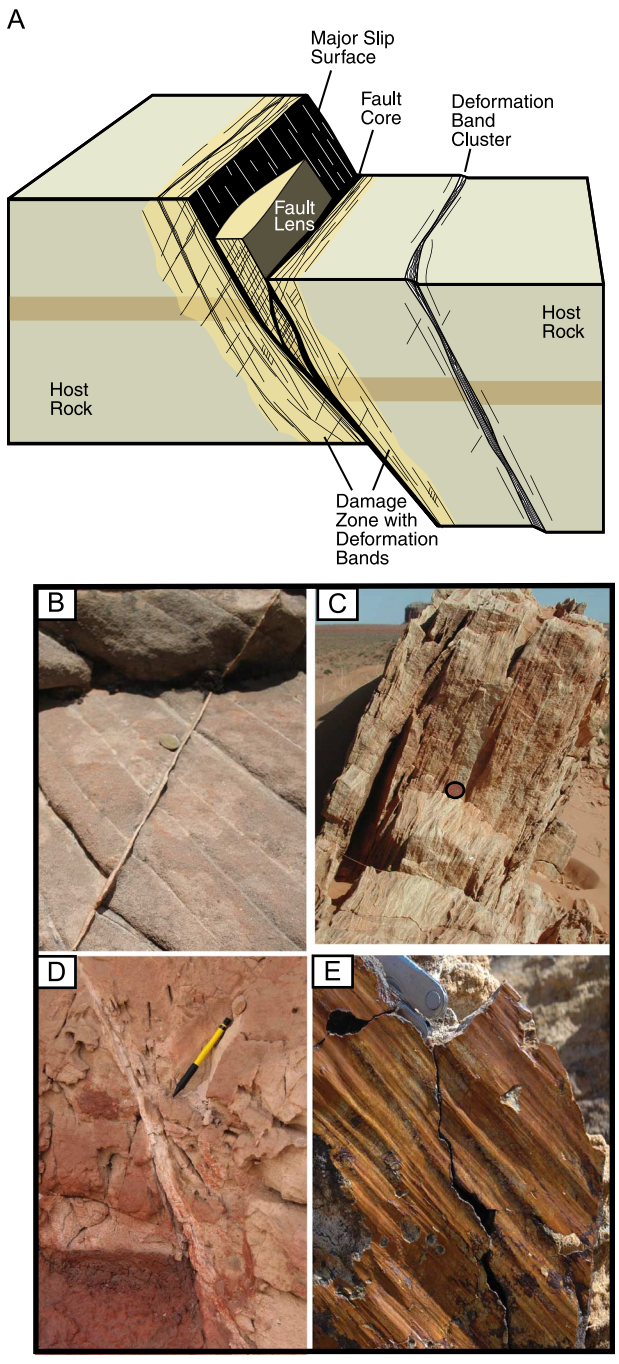

Figure 1. (A) Schematic illustration of fault core and damage zone in sandstone (not to scale); fault core can include the main slip surface, intensively broken and deformed rocks, and lenses of undeformed rocks (host rock). Note the presence of deformation bands in the fault damage zone. (B) Single deformation band (Entrada Sandstone, Utah). (C) Cluster of deformation bands (Entrada Sandstone, Utah). (D) Fault core slip zone (Nubian Sandstone, Sinai). (E) Slip-surface cataclasite (Entrada Sandstone, Utah); see knife for the scale.

edge of the sealing properties of faults, especially in massive sandstones, remains uncertain and necessitates further analyses.

In this study, we use samples from undeformed and deformed sandstones to characterize their petrophysical properties. The results allow for new statistical ways of calculating capillary pressure in a sandstone reservoir with two-phase fluids (e.g., brine [wetting phase] and oil-CO_2 [nonwetting phase]), which are used to calculate the maximum nonwetting-fluid column height that can be sealed as a function of the effective pore-throat radius in the reservoir. Through this study, we validate and expand the empirical relations of Pittman (1992) by applying them on our large fault-related rock data set to very different rock types and by introducing new relations from laboratory measurements.

The approaches introduced in this work will allow geologists to use permeability and/or porosity measurements to estimate the capillary pressures and sealing capacity of different fault-related rocks without requiring direct laboratory measurements of capillary pressure.

DESCRIPTION OF DATA SET

Our samples come from the Entrada Sandstone (Slick Rock and Moab Members) of Utah (United States) and the Nubian sandstones (Malha Formation) of Sinai (Egypt)—two extensive sandstone units that together form a representative range of continental reservoir sandstones. The data sets contain measurements from fault cores (slip zones and slip-surface cataclasite) and damage zone (mainly cataclastic deformation bands). The Slick Rock Member of the Entrada Sandstone (Middle Jurassic) is a subarkose (Table 1) and is composed of thin and laterally discontinuous eolian dune sandstones interbedded with muddy to sandy sabkha and interdune siltstones and sandstones (Foxford et al., 1996). The sandstone is predominantly fine to medium grained and moderately to well sorted. The Moab Member of the Entrada Sandstone (Middle to Upper Jurassic) is a quartz arenite (Table 1) dominated by eolian dunes and is generally better sorted than the Slick Rock Member as it contains fewer

Table 1. X-Ray Diffraction Analyses (X-Ray Diffraction Measured on Powder of Rock Samples in Percent) of the Sandstones Used in This Study*

Sample	Illite/Smectite	Illite+Mica	Kaolinite	Chlorite	Quartz	κ-Feldspar	Plagioclase	Calcite	Dolomite	Siderite	Pyrite	Hematite	Total	Sandstone Type
Malha Formation	0.0	0.0	0.0	0.0	97.2	0.0	TR**	2.3	0.0	0.0	0.0	0.5	100	Quartz arenite
Malha Formation	0.0	0.0	1.6	0.0	98.4	0.0	0.0	TR	0.0	TR	0.0	0.0	100	Quartz arenite
Moab Member	0.0	0.0	0.0	0.0	98.5	1.5	0.0	0.0	0.0	0.0	0.0	0.0	100	Quartz arenite
Slick Rock Member	0.0	3.9	0.0	0.7	79.7	10.3	TR	5.4	TR	TR	TR	TR	100	Subarkose

*Note the interpretations of sandstone types from the x-ray diffraction analyses based on the sandstone classification by Folk (1974).
**TR = trace.

fine grains (Foxford et al., 1996). The maximum burial depth of the Entrada Formation is estimated to be 2.2 km (1.4 mi) by reconstructing the burial and thermal histories of the Paradox Basin (Nuccio and Condon, 1996; Ellingsen, 2011). The latest activity of the Moab fault was reported to be of the early Paleocene based on the age of clay minerals in the damage zone of this fault (Solum et al., 2005). The sandstone of the Malha Formation is a quartz arenite (Table 1) and makes up the uppermost unit of the Nubian Sandstone sequence (Lower Cretaceous, a prerift sequence). This formation consists of fluvial sandstones with gravel lenses and mudstone and kaolinite beds (Moustafa, 2003; Tueckmantel et al., 2010). The Malha Sandstone is moderately sorted and medium to coarse grained. The maximum burial depth of Nubian sandstones at the time of faulting was approximately 1.5 km (0.9 mi) (Du Bernard et al., 2002; Torabi and Fossen, 2009).

In this contribution, we distinguish between deformation bands, dense deformation band clusters (decimeter-wide zones or swarms packed with deformation bands), fault core slip zones, and slip-surface cataclasites, as shown in Figure 1B, C, D, and E. Our distinction of the latter two is based on the slip-surface cataclasites (in walls of well-striated and polished principal slip surfaces) that can be found in the studied units of both Utah and Sinai. In contrast, fault core slip zones have not been described before. Fault core slip zones are encountered in faults with 1- to 10-m offset in some of the Nubian Sandstone units and consist of multiple slip surfaces hosted in variably crushed sandstone. On microscale, the crushed sandstone appears as a poorly sorted mixture of crushed grains enveloping nearly undeformed but slightly rounded host sandstone grains (survivor grains) and mildly deformed sandstone lenses.

SCIENTIFIC APPROACH

Porosity and permeability are two widely used petrophysical properties that can be measured through different approaches and at different sample sizes. In contrast, capillary pressure data are not so commonly found in the geologic literature, mostly because of cost and practicalities. Capillary pressure is the pressure difference between two immiscible fluids that are in contact in a porous media and can be measured by two types of processes: drainage (a nonwetting phase displaces a wetting phase) and imbibition (a wetting phase displaces a nonwetting phase) (Dandekar, 2006). Pittman (1992) presented an inverse approach to empirically calculate capillary pressure for sandstone reservoirs from laboratory-measured porosity and permeability. This method has the potential of providing abundant amounts of inferred capillary pressure data, for example, from cored intervals in a reservoir. In this study, we have implemented the inverse method of Pittman (1992) and, furthermore, used additional approaches to calculate the sealing capacity of our faulted sandstone reservoirs (for details, see approaches A, B, and C in the next section). We use data derived from different methods, including laboratory-measured porosity, absolute permeability, and mercury capillary pressure; in-situ measurements of permeability by minipermeameter (TinyPerm II); and estimated porosity and absolute permeability through image processing of backscatter images of thin sections (Torabi et al., 2008; Torabi and Fossen, 2009).

Capillary Pressure and its Relation to Porosity and Permeability Data

Capillary properties control the magnitude of the differential hydrocarbon buoyancy pressure exerted by a hydrocarbon column, which can be maintained across a lithologic or structural boundary within a reservoir. Thus, capillary pressure and pore-throat size control the ability of a fault to act as a barrier or conduit to hydrocarbon flow on a long-term (geologic) time frame, whereas the permeability of rocks will influence the short (production or injection)-time fluid-flow pattern within a reservoir (Schowalter, 1979; Gibson, 1998). In the inverse method implemented in this study, absolute permeability is used to calculate the capillary pressures of the samples. Among different types of laboratory capillary pressure analyses, the mercury

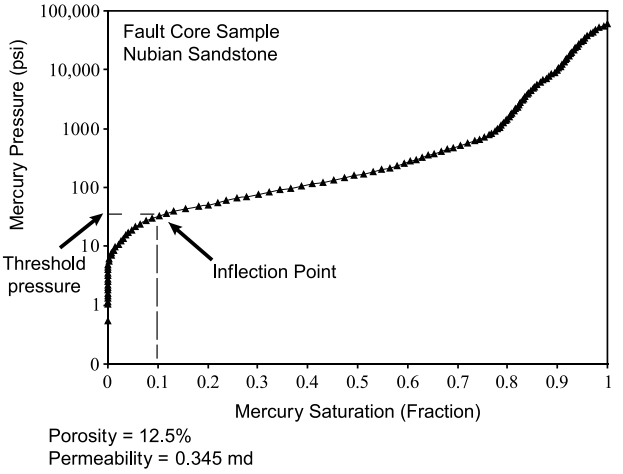

Figure 2. Semilog plot of mercury injection–capillary pressure data for a fault core slip zone sample from the Nubian Sandstone. The threshold pressure corresponds to the inflection point at which the curve becomes convex upward. This is the pressure at which mercury forms a connected pathway through the pores across the sample. 1 psi = 6.9 × 10^{-3} mPa.

injection method is particularly interesting because it can provide insight into the pore-structure and pore-size distributions in a porous medium. Many physical properties of porous rocks are related to their pore characteristics, and hence, their flow characteristics can be evaluated through mercury capillary pressure analysis. In a mercury drainage or injection plot, the pressure at which mercury forms a connected pathway through the pores across the sample is called "threshold pressure," which corresponds to the inflection point (where the curve becomes convex upward) on the plot (Figure 2; Katz and Thompson, 1987; Pittman, 1992). However, the threshold pressure is sometimes difficult to measure (Pittman, 1992).

Some researchers have argued that, in log-log plots of drainage or injection curves, the apex point of the hyperbola (the intersection points of the two asymptotes on the hyperbola) presents an important capillary pressure value, in which the mercury makes a connected pathway (Figure 3A; Thomeer, 1960; Swanson, 1981). Nevertheless, Pittman (1992) commented that not all drainage curves show such an apex point and suggested another way of plotting data for determining the apex point graphically, which he claims to be more accurate than the previously mentioned approaches. He plotted mercury saturation normalized by mercury saturation pressure (*y* axis) against mercury saturation (*x* axis), as shown in Figure 3B. In this study, Pittman's (1992) method has been used to find apex points on the capillary pressure data from 12 samples of deformed and undeformed sandstones (Table 2). Capillary pressure data were obtained through mercury injection into samples performed by Reslab (now Weatherford; for a detailed description of the method, see the Appendix). The analyses were performed on eight samples from fault core slip

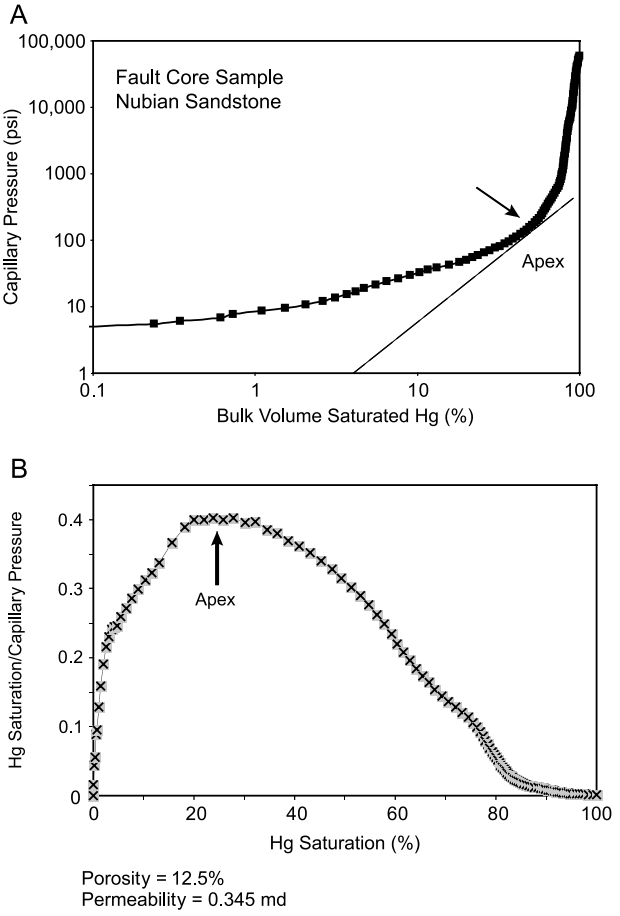

Figure 3. Two different ways to illustrate the apex point for the capillary pressure data of a fault core (slip zone) sample from the Nubian Sandstone. The apex point presents an important capillary pressure, in which the mercury (Hg) makes a connected pathway through the sample. (A) Illustration of the apex point in a log-log plot of drainage or injection curve; the apex point in the resulted hyperbola is the intersection point of the two asymptotes on the hyperbola. (B) Apex point in a plot of normalized mercury saturation versus mercury saturation. The latter illustration has been used to obtain the apex points for all of the samples in this study. 1 psi = 6.9 × 10^{-3} mPa.

Table 2. Laboratory Measurements of Porosity, Permeability, Capillary Pressure, and Pore-Throat Radii and Calculated Values of Capillary Pressure and Pore-Throat Radi*

Sample	Porosity (%)	Permeability (md)	Laboratory Capillary Pressure (psi)	Calculated Capillary Pressure (psi)	Laboratory Pore-Throat Radius (μm)	Calculated Pore-Throat Radius (μm)	*h* (cm)	Calculated *h* (cm)
A	14	23.6	32.50	34.16	2.77	2.64	292.31	307.23
F	18	147	15.16	14.71	5.96	6.14	340.87	132.33
I	16	114	4.88	16.40	18.50	5.50	109.73	147.55
J	12	2.43	58.94	98.84	1.53	0.91	1325.28	888.96
K	11	0.5	70.23	207.34	1.28	0.43	1579.14	1864.87
L	16	125	9.64	15.70	9.38	5.75	216.76	141.25
M	12	31.8	9.64	29.21	9.38	3.08	216.76	262.69
N	15	393	6.14	9.06	14.73	9.97	138.06	81.54
O	17	390	6.86	9.21	13.17	9.81	154.25	82.86
R	14	4.52	70.41	74.77	1.28	1.20	1583.18	672.55
U	29	2465	5.99	4.05	15.08	22.35	134.68	36.44

*The sealing capacity (presented by *h* in the table) of the samples has been calculated through approach A and has been compared to the calculated *h* values through approach B (presented in the last column of this table).

zones of normal faults in the Nubian Sandstone (Malha Formation, Sinai, Egypt; samples I, J, K, L, M, N, R, and T [not listed] in Table 2), two samples from single deformation bands in the Slick Rock Member (samples A and F in Table 2) and one single deformation band sample in the Moab Member (sample O in Table 2) in the damage zone of the Moab fault, and one host rock sample from the Moab fault footwall (Moab Member, Utah, United States; sample U in Table 2). During subsequent quality control of the data, one of the fault core samples (sample T) was excluded because of the poor quality of the laboratory data. Preparation of the samples includes cutting the samples into small pieces (as much as 1.0 cm [0.4 in.]) to keep only the deformed parts of the sample (fault core slip zone or deformation band) and then injecting mercury into the samples. The measured mercury capillary pressure data and the calculated apex points for the different samples were used in the study of empirical relationships between different parameters (see approaches A, B, and C).

Approach A

For the samples with laboratory measurements of mercury capillary pressure and porosity and permeability (Table 2), the following approach has been used:

1. The capillary pressure data are plotted as mercury saturation/capillary pressure versus mercury saturation, and the plot is used to determine the apex of Pittman's (1992) hyperbola (Figure 3B).
2. Then, mercury pressure data are plotted against mercury saturation data, and the capillary pressure at the apex point is identified from the plot. Before using the mercury capillary pressure further, the pressure data have been converted to a reservoir condition for crude oil (<30° API, nonwetting phase) and brine (wetting phase), using the following empirical relationships (Vavra et al., 1992), where σ is the two-phase fluid interfacial tension in millinewtons per meter:

$$P_c = \frac{\sigma_{\text{oil/brine}}}{\sigma_{\text{Hg/air}}} P_{\text{Hg/air}} \quad (1)$$

$$P_c = \frac{31}{485} P_{\text{Hg/air}} \quad (2)$$

3. Based on the Young-Laplace equation for a cylindrical tube model, capillary pressure can be

calculated from the following relationship (Purcell, 1949; Schowalter, 1979):

$$P_c = \frac{2\sigma(\cos\theta)}{r} \qquad (3)$$

where P_c is the capillary pressure at the apex point (dyn/cm^2), r is the effective pore-throat radius, θ is the contact angle between two-phase fluids and solid, and σ is the two-phase fluid interfacial tension (Purcell, 1949; Schowalter, 1979).

The capillary pressure equation can be rewritten in the following form (Schowalter, 1979; Vavra et al., 1992):

$$h = \frac{2\sigma(\cos\theta)}{rg(\Delta\rho)} \qquad (4)$$

where h (cm) is the maximum hydrocarbon fluid column height that can be sealed as a function of the effective pore-throat radius (r), $\Delta\rho$ (g/cm^3) is the difference between the density of the two-phase fluids in contact within rock pore throats (in this study, brine and oil), and g is the acceleration of gravity (980 cm/s^2 [386 in./s^2]).

From combining equations 3 and 4, we get

$$h = \frac{P_c}{g(\Delta\rho)} \qquad (5)$$

where h (the fluid column height) can be easily calculated by having capillary pressure at the apex point as the main variable.

Approach B

For other samples (core-plug samples and other measurements obtained through image processing of backscatter images of thin sections) from which only porosity and permeability data were available, the following approach has been used:

1. The empirical relationship between porosity (ϕ), permeability (k), and pore-throat radius at apex point (r_{apex}, effective pore throat) found by Pittman (1992) was used (equation 6; R^2 is the coefficient of determination). This empirical relationship is based on measurements (core-plug porosity and permeability and capillary mercury injection) on more than 200 undeformed sandstone samples from 14 different formations (Pittman, 1992):

$$\log r_{apex} = -0.117 + 0.475\log k - 0.099\log\phi \qquad R^2 = 0.91 \qquad (6)$$

2. From the previous capillary pressure data (Table 2), r_{apex} data were plotted against capillary pressure data at apex points, and the statistical relationship between the two (equation 7) is used for calculation of capillary pressure at apex points for pore-throat radii obtained by equation 6 (Figure 4). The calculated capillary pressure data are then converted to a reservoir condition (brine and oil) using equation 2.

$$P_c = 90.018(r)^{-0.99} \qquad R^2 = 1 \qquad (7)$$

3. The maximum nonwetting-fluid column height (h, the height of sealed hydrocarbon) that can be stored in the samples can be calculated from equation 5, assuming a two-phase fluid in a reservoir condition (e.g., brine and oil).

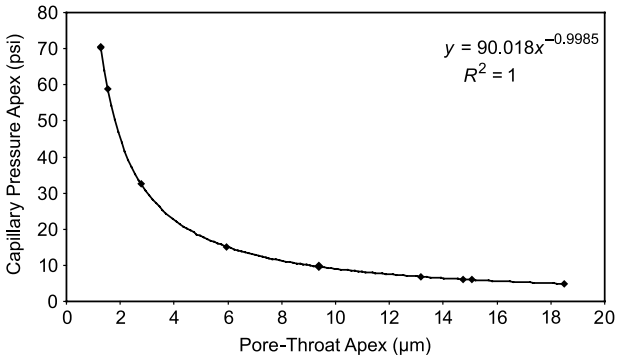

Figure 4. Correlation between capillary pressures at apex points and their related pore throats for mercury-injected samples.

Approach C

For samples from outcrops that only offered permeability measurements from minipermeameter data, the following approach was used:

1. The porosity term has been found to be without significance in equation 6 (Pittman, 1992).

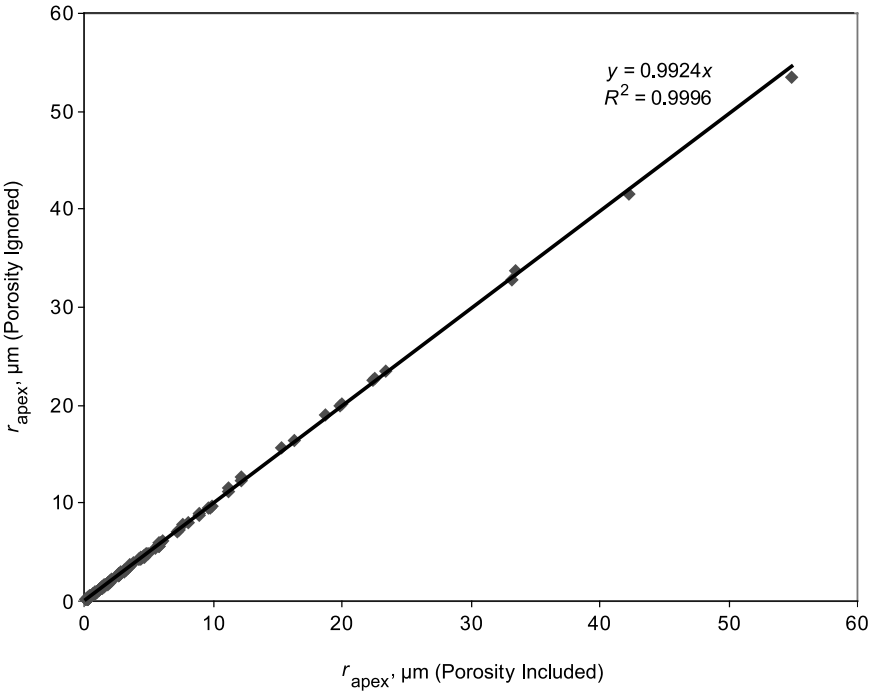

Figure 5. Pore throat radius at apex points (r_{apx}) have been calculated by including porosity (x axis) and removing porosity (y axis) for core-plug data. The plot shows that porosity is not significant in the calculation.

To further test this finding, we have examined the significance of porosity in our calculations and found that the differences are small and of little significance (Figure 5). Therefore, a regression (equation 8) that does not include porosity as a variable has been used to calculate pore-throat radius at apex points. This regression was made by correlating our laboratory-measured permeability and pore-throat radii at apex points. However, Pittman (1992) has suggested a different relationship between these two parameters (equation 9), which, when applied to our data, results in a slightly higher pore throat than what we get from equation 8.

$$\log r_{apx} = 0.123 + 0.37 \log k \qquad R^2 = 0.80 \tag{8}$$

$$\log r_{apx} = -0.226 + 0.466 \log k \qquad R^2 = 0.90 \tag{9}$$

2. Equation 7 has been used to calculate the capillary pressures at the apex points. The calculated capillary pressures are then converted to a reservoir condition (brine and oil) using equation 2.
3. The maximum nonwetting-fluid column height (h) that can be stored in the samples can be calculated from equation 5 assuming a two-phase fluid in a reservoir condition (brine and oil).

RESULTS

Permeability-Porosity Relationships

In addition to the porosity and permeability data of the samples used in mercury injection experiments (Table 2), we make use of an extensive porosity-permeability database based on other types of measurements (core plug and image processing of thin sections), as shown in Figure 6. The rocks used for these measurements include the sandstones from the same or similar units as those presented in Table 1. The relationship between porosity and permeability data from core-plug measurements of a host rock, a single deformation band, a cluster of deformation bands, and fault core slip zones have been studied (Figure 6A). The results show that, for all of the samples, this relationship fits a robust power law but that the power-law exponent (D) depends on the degree of deformation experienced

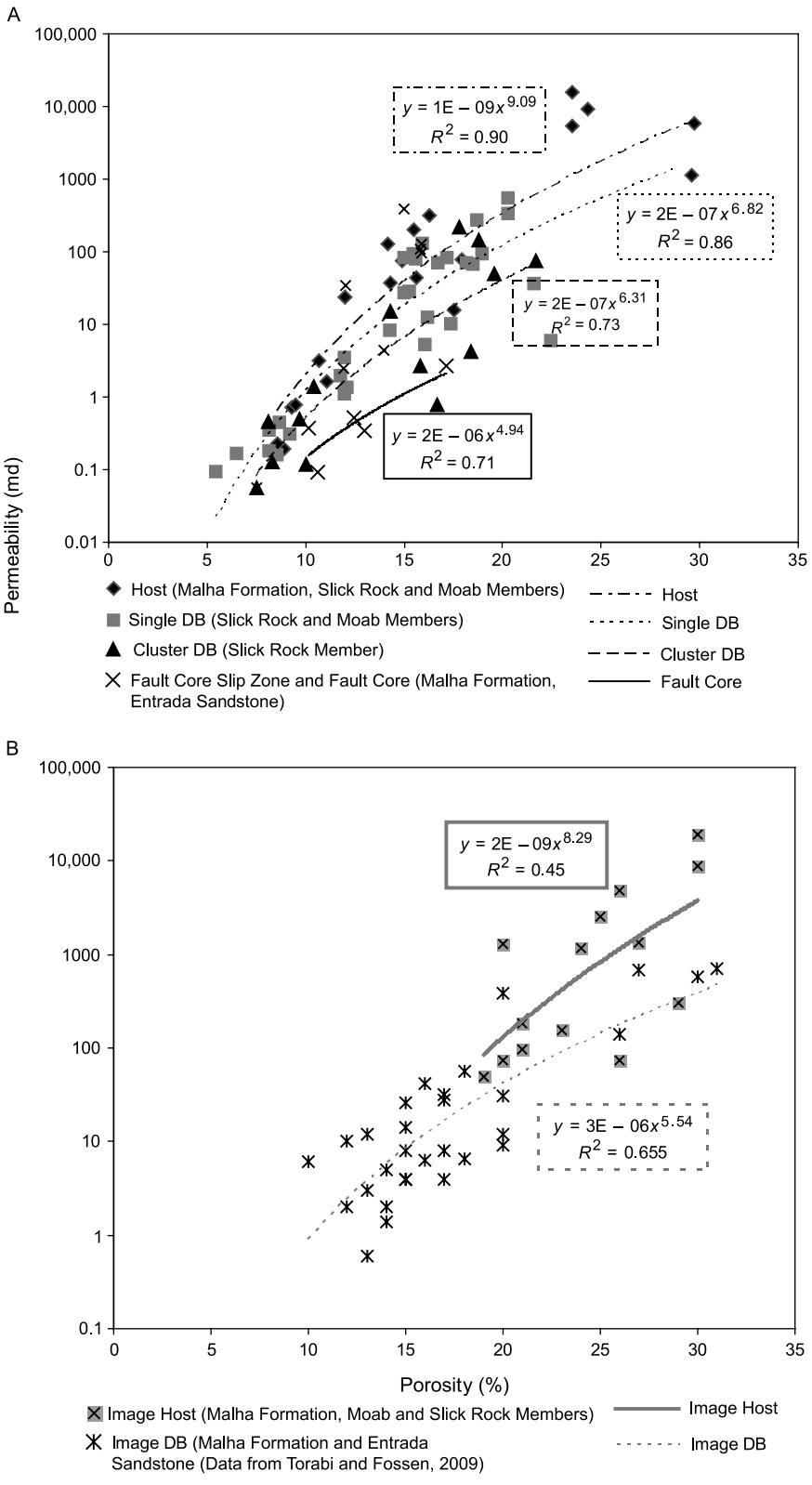

Figure 6. Permeability-porosity relationship for all of the samples. Permeability-porosity relationship for core-plug samples (host rock, single deformation band (DB), cluster of DBs, and fault core slip zone) (A) and for host rock and single DBs from image processing of thin sections (B). The fitted curves to the data are power laws. The power-law exponent decreases as the degree of deformation increases in the samples.

by the samples. More specifically, D ranges from approximately 9 for the host rock samples to approximately 5 for the fault core samples (Figure 6A). Furthermore, for a given porosity, host rock samples have higher permeability than deformed rocks, and the permeability at a given porosity decreases

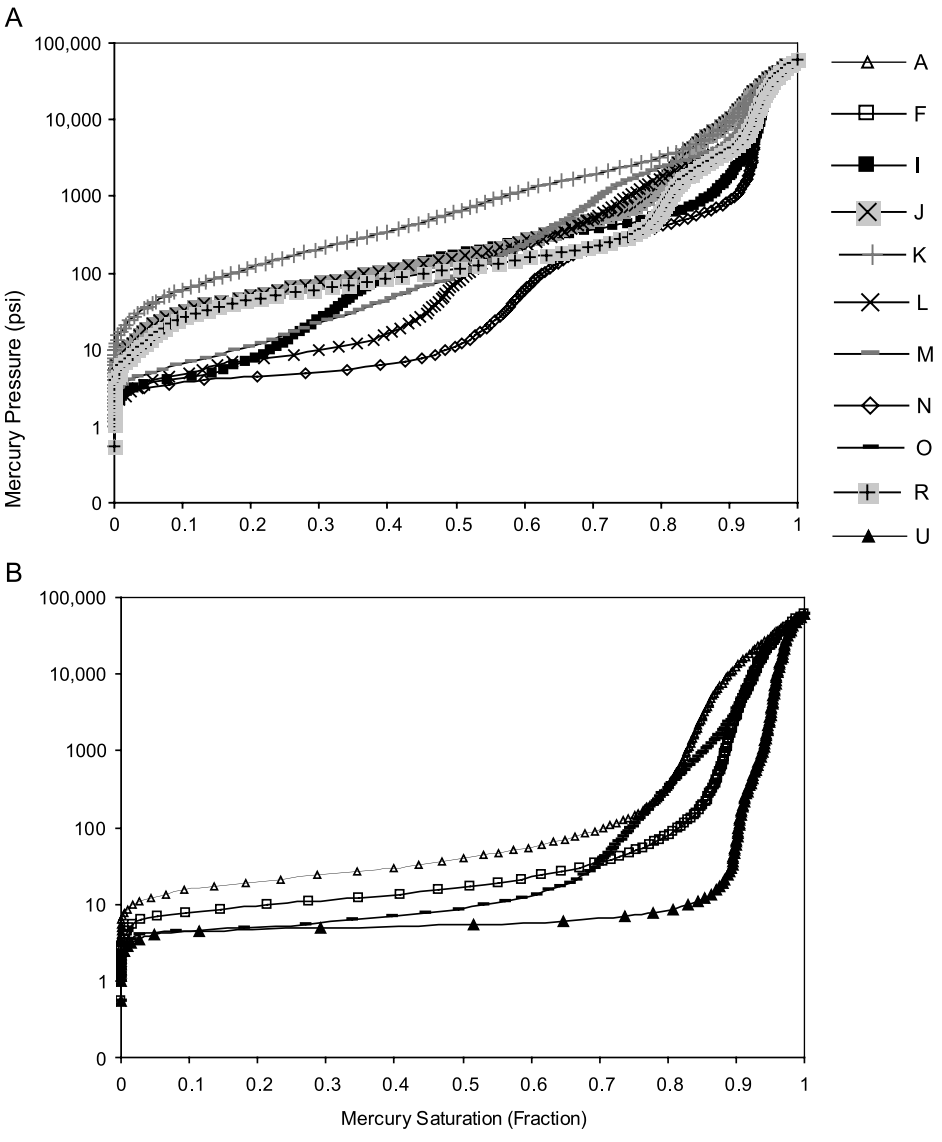

Figure 7. Comparison of the semilog drainage (injection) plots for mercury-injected samples reveals that the drainage curve for fault core slip zone samples is different from those of deformation band and host rock samples. (A) The drainage curve for fault core slip zone samples for most of the samples has more than one inflection point. (B) The deformation band and host rock samples follow almost a standard drainage curve after the inflection points, with some slight changes in high capillary pressures. Samples are presented in Table 2. 1 psi = 6.9×10^{-3} mPa.

with the amount of deformation (Figure 6A). A similar relationship can be obtained from permeability-porosity data estimated through image processing of the thin sections (Figure 6B), although the exponents are slightly different from those obtained for core-plug samples and are also less well defined. This is because the measured sample size was smaller than that of the core plugs. This is particularly true for deformation bands, where we measured only the properties of the bands with no part of the host rock included (Torabi et al., 2008). Therefore, the deformation band porosity and permeability values estimated from image processing are slightly lower than the values that are obtained from core plugs (Figure 6B).

Capillary Pressure Measurements

Detailed information on the properties of the samples used in mercury injection experiments are provided in Table 2. The laboratory mercury capillary pressure and pore-throat radii of the samples (approach A) are compared to the calculated capillary pressure and pore-throat radii (approach B) of the same samples in Table 2. A comparison of the semilog drainage (injection) plots (Figure 7A, B) for our mercury capillary pressure measurements reveals that the drainage curves for fault core slip zone samples are different from those of deformation band and host rock samples. The deformation band and host rock samples closely

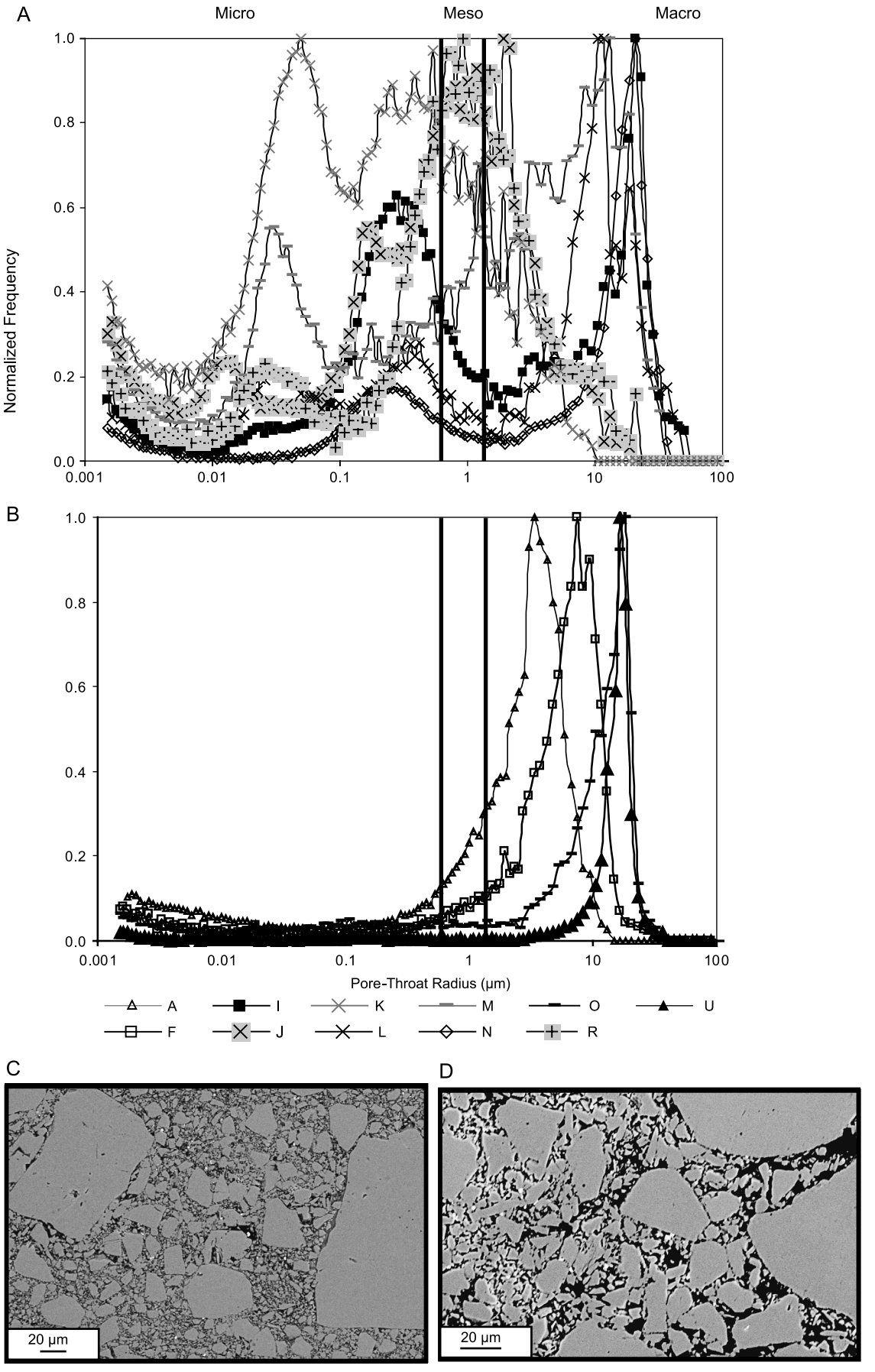
A
Micro
Meso
Macro
Normalized Frequency
1.0
0.8
0.6
0.4
0.2
0.0
0.001
0.01
0.1
1
10
100
B
Pore-Throat Radius (μm)
A
I
K
M
O
U
F
J
L
N
R
C
20 μm
D
20 μm

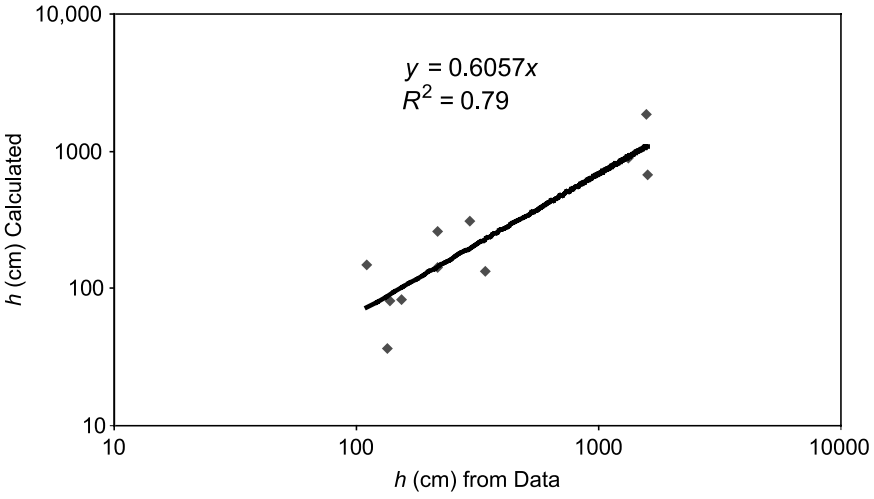

Figure 9. Correlation between calculated fluid column height (*h*) values through approach B and calculated *h* values directly for mercury injection data (*x* axis, approach A) for the same samples (in Table 2). The resulting equation has been used to calibrate the data calculated through approaches B and C.

follow a standard drainage curve after the inflection points, with some slight changes in high capillary pressures (Figure 7B). In contrast, the drainage curve for fault core slip zone samples has more than one inflection point (Figure 7A) for most of the samples. This is also evident from Figure 8, where the pore-size distributions for fault core slip zone samples show a bimodal pattern (Figure 8A). This pattern reflects poorly sorted grain size, with crushed grains enveloping undeformed host rock grains and mildly deformed lenses (Figure 8C, D).

The maximum nonwetting fluid (oil in our studied samples) column height (*h*) that can be stored in the samples because of their induced capillary pressure has been calculated for all the samples using equation 5, assuming minimum densities for oil and brine in the reservoir based on the typical range of oil-field fluids (i.e., $\rho_{oil} = 0.51$ g/cm^3 and $\rho_{brine} = 1$ g/cm^3; Vavra et al., 1992). For the same samples (samples in Table 2), the *h* values that have been calculated through approach B in the methodology section have been correlated with the *h* values calculated directly from the laboratory data (approach A in the approach section) in Figure 9. The resulting equation (Figure 9) was further used to calibrate all the *h* values calculated through approaches B and C. The plotted calibrated *h* values in Figure 10A suggest that even a single deformation band can, from a theoretical point of view, withhold more than 60 m (197 ft) of oil column in the extreme case. The sealing capacity of deformation bands increases (they can theoretically withhold more than 80 m [262 ft] of oil column) when they form clusters of bands (Slick Rock Member data in Figure 10A) because their influence on fluid flow is related to the accumulated properties of the bands. Although the average estimated seal capacity of fault core slip zone samples (Nubian Malha Formation) is higher than any other sample on the graph (>140 m [459 ft] in the extreme case; Figure 10A), the data suggest that a cluster of deformation bands can locally affect fluid flow to the same extent as a fault core slip zone. The host rock and single deformation band data from image processing of thin sections are in the range of the data obtained from fault core plugs, although they exhibit slightly lower values of *h* (Figure 10A). The single deformation bands (image processing) can obviously seal higher amounts of fluid than their corresponding host rocks (Figure 10A). The comparison of *h* values obtained from minipermeameter data (Figure 10B; approach C in the methodology) with the other data in Figure 10 is not straightforward because the range of permeability values measured in situ

Figure 8. Distribution of pore-throat size in the mercury-injected samples (Table 2): for fault core slip zone samples at which most of them show bimodal distribution (A) and for deformation bands and host rock (B). (C and D) Examples of microstructure of fault core slip zone samples (samples I and L, respectively, in backscatter images), which reflect the heterogeneous (bimodal) grain-size distribution (a mixture of crushed grains and nearly undeformed host rock grains [survivor grains] and mildly deformed lenses trapped between the mostly crushed grains) within these samples.

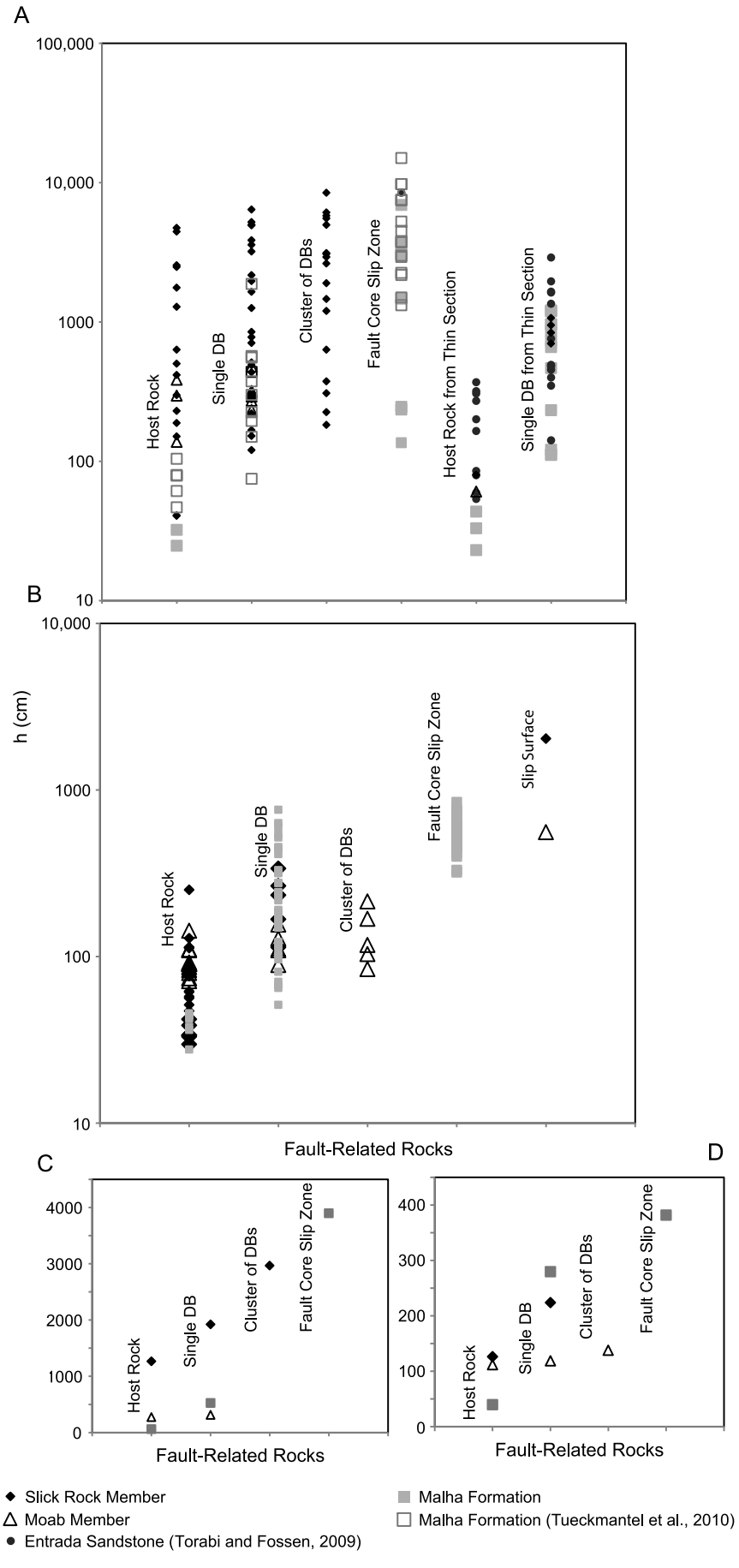

Figure 10. Sealing capacity of different fault-related rocks presented by fluid column height (*h*) values (the column height of hydrocarbon that could be stored because of the capillary pressure induced by these rocks) using calibrated capillary pressure values for host rock, single deformation band (DB), cluster of DBs, fault core slip zone samples (processed through approaches A and B). Clusters of DBs and fault core slip zones data show high sealing capacity, although fault core slip zones present the highest *h* values. The data presented by the open gray squares were calculated from the mercury capillary pressure values for the Nubian Sandstone (Malha Formation) in Sinai (the original capillary pressure data are from Tueckmantel et al., 2010) (A); and *h* values were calculated through approach C for data from in-situ measurements of permeability from mini-permeameter data. The data are in the lower range in comparison to the other data in the upper plot. Fault core slip zones show the highest values of *h* in comparison to the other samples in this plot, although the values are almost one-tenth of the *h* values in A (B). (C and D) Averaged *h* values for the sample showing a range of *h* values in plots A and B of this figure, respectively.

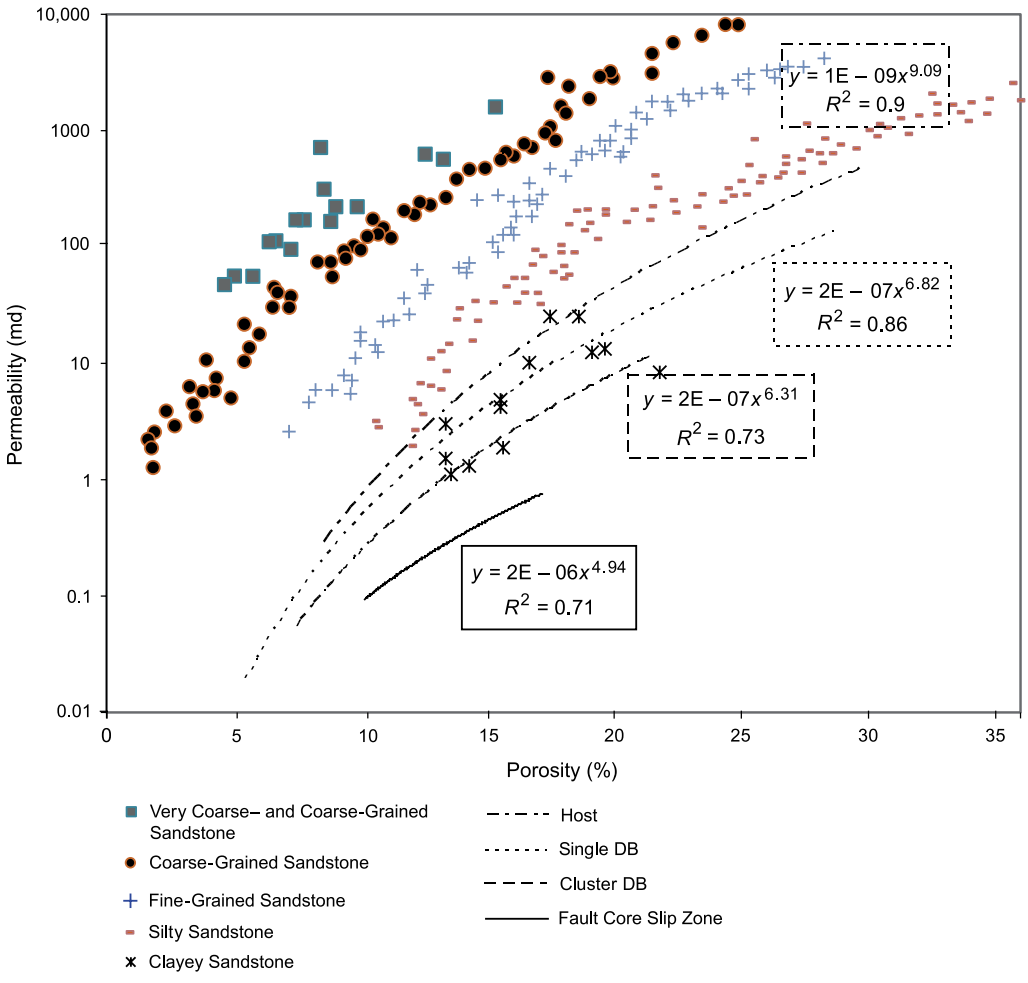

Figure 11. Comparison of the permeability-porosity relationship between the fault rock data from this study and the published data of sandstones with different grain sizes (very coarse– to coarse-grained, coarse- to medium-grained, fine-grained, silty, and clayey sandstones; the original data are from Chilingarian, 1963); both types of data show similar trends, although the permeability values are higher in the published data (undeformed sandstone). Note the increasing *D* values (power-law exponent) from fault-related rocks to host rock implying increasing permeability toward the host rock. DB = deformation band.

in the field almost doubles laboratory measurements of the same rocks (Fossen et al., 2011). This deviation is especially seen as the minipermeameter approaches its lower threshold in range (minimum of 10 md for instrument). In general, the *h* values calculated from minipermeameter data (Figure 10B) are substantially less than the *h* values obtained for the same type of fault rocks in core-plug samples (almost one-tenth of the *h* values in Figure 10A). In Figure 10B, fault core slip zones and single deformation bands from the Nubian Sandstone (Malha Formation) show a higher sealing capacity than their corresponding host rocks. For Moab Member samples, the sealing capacity of a cluster of deformation bands and the single data from slip-surface cataclasite is higher than that of single deformation band and host rock samples (Figure 10B). The comparison of *h* values for Slick Rock Member samples shows a very clear increase from host rock to single band and to the slip-surface cataclasite data, although we have only one data point for the slip surface (Figure 10B). Hence, the two data sources give quantitatively similar results overall. In Figure 10C and D, the averaged *h* values for the samples that show a range of *h* values for each specific fault-related rock in Figure 10A and B are presented, respectively. The comparison of these plots confirms that the fault core slip zone presents the highest sealing capacity among the different fault rocks presented in Figure 10.

DISCUSSION

Establishing a global quantitative relationship between the porosity and permeability data of sandstones is challenging because the grain size and grain-size distribution of sandstones affect this

relationship (Chilingarian, 1963). Previous studies of sandstones with different grain sizes (Chilingarian, 1963; Tiab and Donaldson, 2004; Figure 11) show that very coarse– to coarse-grained, coarse- to medium-grained, fine-grained, silty, and clayey sandstones show parallel trends in the permeability-porosity relationship, although no regression has been made on the data. However, the modified version of the Kozeny-Carman relationship (Walsh and Brace, 1984) that is used for porous media (undeformed rocks) is based on the dependence of permeability (k) on porosity (ϕ), the specific surface area of the pore-grain interface (s, as an indicator of grain size), and the formation factor (F), which again is related to porosity and to c, which is a constant related to pore geometry that is equal to 2 for materials possessing pores of circular cross section.

$$k = \phi^2 / cFs^{-2}$$

The new regressions that we have applied to our data involve only permeability and porosity as variables and therefore allow for a straightforward prediction of either of these two parameters from the other, depending on the type of fault-related rocks. The comparison of our results (the power-law regressions drawn on the data) with previously published data (Tiab and Donaldson, 2004) shows some agreement in the permeability-porosity relationships, although the permeability values are, in general, higher in the previously published data from undeformed sandstones (Figure 11). An increase in permeability from fine- to coarse-grained sandstone is observed. Similarly, our data show an increase in permeability from fault-related rocks (fault core slip zone and deformation bands) to the host rock, which is shown by an increase in the D value from approximately 5 to approximately 9, respectively.

In general, the trend of published data is similar to the regressions made on our data (Figure 11). For a given porosity, permeability is higher in host rock samples and decreases with deformation (Figure 6). This is so because the microstructure of the host rock and cataclastic bands is controlled by different processes. Within cataclastic bands, grain crushing results in more angular grains and a different grain-size distribution compared to the compacted host sandstone. As a result, the specific surface area at pore-grain contacts increases, which in turn causes more reduction in permeability than in porosity (Torabi and Fossen, 2009). Our results show that fault core slip zones are the most efficient barriers to flow in comparison to the other fault rocks studied in this work, with a calculated sealing capacity exceeding 140 m (459 ft) of oil in the extreme case (Figure 10). However, deformation bands can locally offer capillary pressures comparable to fault core slip zones and slip surfaces (Figure 10). Note that both single deformation band and clusters of bands are heterogeneous in the sense that their thickness and microtexture and hence their petrophysical properties can substantially change over a short distance (Torabi and Fossen, 2009). Because the current estimates are based on measurements at the millimeter-to-centimeter scale, the effective sealing effects of such structures in a reservoir setting may be considerably lower. Note that the latter depends strongly on the arrangement and connectivity of deformation bands and cluster zones. Hence, deformation bands or clusters that do not form completely continuous structures or zones across fault blocks in a hydrocarbon reservoir will, of course, not have sealing properties close to the theoretical values presented here.

Regarding the fault core slip zones in general, the presented method is not directly dependent on fault rock thickness, although it is expected that the thicker the core, the better the chance for continuity of the seal. When it comes to the microstructural details of the fault core, different fault features could have different effects on the properties of faults. For example, sandstone fault lenses in otherwise highly cataclastic sandstone commonly have less impact on the petrophysical properties of faults in comparison to the surrounding fault rocks, because they contain remnants of undeformed or mildly deformed rocks. In contrast, fluid flow perpendicular to slip surfaces can be substantially hindered because of considerable permeability reduction (Figure 10A, B).

In this study, we have converted mercury capillary pressures to a reservoir condition (brine and oil). If we consider brine and CO_2 as two phases in an aquifer, the interfacial tension between CO_2 and

brine (in the range of 20–40 mNm^{-1}) will control the resulting capillary pressure because the interfacial tension has shown a pronounced dependence on pressure and temperatures in the experiments run on brine and CO_2 (e.g., Kvamme et al., 2007; Angeli et al., 2009). Depending on the selected interfacial tension (σ) for brine and CO_2 ($\sigma_{min} = 20\,mNm^{-1}$ and $\sigma_{max} = 40\,mNm^{-1}$; Angeli et al., 2009), the corresponding capillary pressure changes. A higher interfacial tension results in higher capillary pressure values in the brine and CO_2 system for the same samples. This in turn will affect the maximum height of the CO_2 column that can be stored through capillary forces.

Among the different trapping mechanisms involved in the sequestration process of CO_2, the capillary trapping mechanism could be the most effective (Wildenschild et al., 2011). In contrast to the mercury capillary experiments discussed in this study, capillary trapping of CO_2 commonly occurs during the imbibition of brine, when CO_2 is migrating upward and brine imbibes back into the formation because of density difference (buoyancy forces), after the injection of CO_2 has stopped. At the imbibition process, the capillary pressure (residual or minimum capillary pressure) locks CO_2 at the pore scale and hence inhibits large-scale movement of CO_2 within the aquifer (Wildenschild et al., 2011).

CONCLUSIONS

This study focuses mainly on the properties of fault-related rocks in clean sandstones, that is, without significant clay minerals. We have studied samples of host rock, deformation bands, fault core slip zones, and slip-surface cataclasite from the Entrada Sandstone (Slick Rock and Moab Members) and Nubian sandstones (Malha Formation). Our results show the following:

1. Power-law regressions can be fitted to the porosity-permeability data obtained through laboratory measurements. The D has a reduction from host rock (D, ~9) to fault core (D, ~5) in accordance with the increasing strain experienced by the samples. For a given porosity, permeability is higher in host rock samples than in deformed samples and will decrease with the degree of deformation in the samples.
2. The approaches introduced in this work will allow geologists to use in-situ (field), core-plug, and thin section (image processing) measurements of permeability and/or porosity to estimate the capillary pressures and sealing capacity of different fault-related rocks without requiring direct laboratory measurements of capillary pressure.
3. The sealing capacity of fault core slip zone was found to be higher than that of single deformation bands and clusters of bands. Our calculations suggest that a fault core slip zone offers more than 140-m (459-ft) height of hydrocarbon in extreme cases. A cluster of deformation bands can locally act as efficiently as a fault core slip zone or slip-surface cataclasite in increasing capillary pressure and sealing the nonwetting fluid.
4. A higher interfacial tension between brine and CO_2 in a brine and CO_2 system will result in a higher capillary pressure and sealing capacity for the same samples when compared to a brine and oil system.

APPENDIX: MERCURY INJECTION METHOD

The main components of the mercury injection apparatus are a mercury pump for injection, a chamber to house the sample, pressure gauges, and devices for volume measurements. A sample with a known porosity and permeability is placed into the selected penetrometers in the mercury chamber and is completely evacuated before the mercury is injected into it. The injected mercury represents the nonwetting phase, the volume of which increases with increasing pressure until the sample is saturated by mercury (Dandekar, 2006). In the instrument used for the mercury injection at Reslab (Autopore IV 9520), initially, several pressure steps are defined in a pressure table over a range from vacuum to 60,000 psi (414 mPa). The Autopore software automatically takes readings between points on the pressure table until the maximum level of intrusion is detected. This maximum intrusion is also predetermined based on the petrophysical parameters of the sample and is presented in milliliters of mercury per gram of the sample. The pressures and saturations measured during the experiments make the drainage capillary pressure–saturation curve. The volume of mercury

in the penetrometer stem is measured by determining the penetrometer's electrical capacitance. The data are further analyzed using the Young-Laplace equation.

REFERENCES CITED

Angeli, M., M. Soldal, E. Skurtveit, and E. Aker, 2009, Experimental percolation of supercritical CO_2 through a caprock: Energy Procedia, v. 1, p. 3351–3358, doi:10.1016/j.egypro.2009.02.123.

Antonellini, M., and A. Aydin, 1994, Effect of faulting on fluid flow in porous sandstones: Petrophysical properties: AAPG Bulletin, v. 78, p. 355–377.

Braathen, A., J. Tveranger, H. Fossen, T. Skar, N. Cardozo, S. E. Semshaug, E. Bastesen, and E. Sverdrup, 2009, Fault facies and its application to sandstone reservoirs: AAPG Bulletin, v. 93, p. 891–917, doi:10.1306/03230908116.

Caine, J. S., J. P. Evans, and C. B. Forster, 1996, Fault zone architecture and permeability structure: Geology, v. 24, p. 1025–1028, doi:10.1130/0091-7613(1996)024<1025:FZAAPS>2.3.CO;2.

Chester, F. M., and J. M. Logan, 1986, Implications for mechanical properties of brittle faults from observations of the Punchbowl fault zone, California: Pure and Applied Geophysics, v. 124, p. 79–106, doi:10.1007/BF00875720.

Childs, C., J. J. Walsh, T. Manzocchi, J. Strand, A. Nicol, M. Tomasso, M. P. J. Schöpfer, and A. Aplin, 2007, Definition of a fault permeability predictor from outcrop studies of a faulted turbidite sequence, Taranaki, New Zealand, *in* S. J. Jolley, D. Barr, J. J. Walsh, and R. J. Knipe, eds., Structurally complex reservoirs: Geological Society (London) Special Publication 292, p. 235–258.

Chilingarian, G. V., 1963, Relationships between porosity, permeability and grain size distribution of sands and sandstones, *in* J. U. van Straaten, ed., Deltaic and shallow marine deposits: New York, Amsterdam, Elsevier Science Publishing Company, p. 71–75.

Dandekar, A. Y., 2006, Petroleum reservoir rocks and fluid properties: Boca Raton, Florida, Taylor & Francis Group, 460 p.

Du Bernard, X. D., P. Eichhubl, and A. Aydin, 2002, Dilation bands: A new form of localized failure in granular media: Geophysical Research Letters, v. 29, p. 2176–2179, doi:10.1029/2002GL015966.

Ellingsen, E., 2011, Interaction of diagenesis and deformation of faulted sandstone reservoirs: Master's thesis, University of Bergen, Bergen, Norway, 152 p.

Færseth, R., 2006, Shale smear along large faults: Continuity of smear and the fault seal capacity: Journal of the Geological Society (London), v. 163, p. 741–751, doi:10.1144/0016-76492005-162.

Fisher, Q. J., and R. J. Knipe, 1998, Fault sealing processes in siliciclastic sediments, *in* G. Jones, Q. J. Fisher, and R. J. Knipe, eds., Faulting and fault sealing in hydrocarbon reservoirs: Geological Society (London) Special Publication 147, p. 117–134.

Fisher, Q. J., and R. J. Knipe, 2001, The permeability of faults within siliciclastic petroleum reservoirs of the North Sea and Norwegian continental shelf: Marine and Petroleum Geology, v. 18, p. 1063–1081, doi:10.1016/S0264-8172(01)00042-3.

Fisher, Q. J., S. D. Harris, E. McAllister, R. J. Knipe, and A. J. Bolton, 2001, Hydrocarbon flow across sealing faults: Theoretical constraints: Marine and Petroleum Geology, v. 18, p. 251–257, doi:10.1016/S0264-8172(00)00064-7.

Folk, R. L., 1974, Petrology of sedimentary rocks: Austin, Texas, Hemphills, 182 p.

Fossen, H., R. A. Schultz, K. Mair, and Z. Shipton, 2007, Deformation bands in sandstones: A review: Journal of Geological Society (London), v. 164, p. 755–769, doi:10.1144/0016-76492006-036.

Fossen, H., R. A. Schultz, and A. Torabi, 2011, Conditions and implications for compaction band formation in the Navajo Sandstone, Utah: Journal of Structural Geology, v. 33, p. 1477–1490, doi:10.1016/j.jsg.2011.08.001.

Foxford, K. A., I. R. Garden, S. C. Guscott, S. D. Burley, J. J. M. Lewis, J. J. Walsh, and J. Watterson, 1996, The field geology of the Moab fault, *in* A. C. Huffman Jr., W. R. Lund, and L. H. Godwin, eds., Geology and resources of the Paradox Basin: Utah Geological Association Guidebook 25, p. 265–283.

Gibson, R. G., 1994, Fault-zone seals in siliciclastic strata of the Columbus Basin, offshore Trinidad: AAPG Bulletin, v. 78, p. 1372–1385.

Gibson, R. G., 1998, Physical character and fluid flow properties of sandstone-derived fault zones, *in* M. P. Coward, T. S. Daltaban, and H. Johnson, eds., Structural geology in reservoir characterization: Geological Society (London) Special Publication 127, p. 83–98.

Jolley, S. J., D. Barr, J. J. Walsh, and R. J. Knipe, 2007, Structurally complex reservoirs: An introduction, *in* S. J. Jolley, D. Barr, J. J. Walsh, and R. J. Knipe, eds., in Structurally complex reservoirs: Geological Society (London) Special Publication 292, p. 1–24.

Katz, A. J., and A. H., Thompson, 1987, Quantitative prediction of permeability in porous rock: Physical Review B, v. 34, p. 8179–8181, doi:10.1103/PhysRevB.34.8179.

Knipe, R. J., 1997, Juxtaposition and seal diagrams to help analyze fault seals in hydrocarbon reservoirs: AAPG Bulletin, v. 81, p. 187–195.

Kvamme, B., T. Kuznetsova, A. Hebach, A. Oberhof, and E. Lunde, 2007, Measurements and modeling of interfacial tension for water + carbon dioxide systems at elevated pressures: Computational Materials Science, v. 38, p. 506–513, doi:10.1016/j.commatsci.2006.01.020.

Manzocchi, T., C. Childs, and J. J. Walsh, 2010, Faults and fault properties in hydrocarbon flow models: Geofluids, v. 10, p. 94–113.

Moustafa, A. R., 2003, Explanatory notes for the geologic maps of the eastern side of the Suez Rift (western Sinai Peninsula): Cairo, Egypt, AAPG/Datapages GIS Series, 34 p.

Nuccio, V. F., and S. M. Condon, 1996, Burial and thermal history of the Paradox Basin, Utah and Colorado, and petroleum potential of the Middle Pennsylvanian Paradox Formation: U.S. Geological Survey Bulletin 2000-O, 47 p.

Peacock, D. C. P., R. J. Knipe, and D. J. Sanderson, 2000, Glossary of normal faults: Journal of Structural Geology, v. 22, p. 291–305, doi:10.1016/S0191-8141(00)80102-9.

Pittman, E. D., 1992, Relationship of porosity and permeability to various parameters derived from mercury injection: Capillary pressure curves for sandstone: AAPG Bulletin, v. 76, p. 191–198.

Purcell, W. R., 1949, Capillary pressures: Their measurement using mercury and the calculation of permeability therefrom: American Institute of Mechanical Engineers Petroleum Transactions, v. 1, no. 2, p. 39–48.

Schowalter, T. T., 1979, Mechanism of secondary hydrocarbon migration and entrapment: AAPG Bulletin, v. 63, p. 723–760.

Schultz, R. A., and H. Fossen, 2008, Terminology for structural discontinuities: AAPG Bulletin, v. 92, p. 853–867, doi:10.1306/02200807065.

Shipton, Z. K., and P. A. Cowie, 2003, A conceptual model for the origin of fault damage zone structures in high-porosity sandstone: Journal of Structural Geology, v. 25, p. 333–345, doi:10.1016/S0191-8141(02)00037-8.

Solum, J. G., B. A. van der Pluijm, and D. R. Peacor, 2005, Neocrystalization, fabrics and age of clay minerals from an exposure of the Moab fault, Utah: Journal of Structural Geology, v. 27, p. 1563–1576, doi:10.1016/j.jsg.2005.05.002.

Smith, D. A., 1966, Theoretical consideration of sealing and nonsealing faults: AAPG Bulletin, v. 50, p. 363–374.

Sternlof, K. R., J. R. Chapin, D. D. Pollard, and L. J. Durlofsky, 2004, Permeability effects of deformation band arrays in sandstone: AAPG Bulletin, v. 88, p. 1315–1329.

Swanson, B. F., 1981, A simple correlation between permeabilities and mercury capillary pressures: Journal of Petroleum Technology, v. 33, p. 2498–2504.

Tiab, D., and E. C. Donaldson, 2004, Petrophysics, 2d ed.: New York, Elsevier, 881 p.

Thomeer, J. H. M., 1960, Introduction of a pore geometrical factor defined by the capillary pressure curve: Journal of Petroleum Technology, v. 12, no. 3, p. 73–77.

Torabi, A., and S. S. Berg, 2011, Scaling of fault attributes: A review: Marine and Petroleum Geology, v. 28, p. 1444–1460, doi:10.1016/j.marpetgeo.2011.04.003.

Torabi, A., and H. Fossen, 2009, Spatial variation of microstructure and petrophysical properties along deformation bands in reservoir sandstones: AAPG Bulletin, v. 93, p. 919–938, doi:10.1306/03270908161.

Torabi, A., H. Fossen, and B. Alaei, 2008, Application of spatial correlation functions in permeability estimation of deformation bands in porous rocks: Journal of Geophysical Research, v. 113, p. 1–10, doi:10.1029/2007JB005455.

Tueckmantel, C., Q. J. Fisher, R. J. Knipe, H. Lickorish, and S. M. Khalil, 2010, Fault seal prediction of seismic-scale normal faults in porous sandstone: A case study from the eastern Gulf of Suez rift, Egypt: Marine and Petroleum Geology, v. 27, p. 334–350, doi:10.1016/j.marpetgeo.2009.10.008.

Vavra, C. L., J. G. Kaldi, and R. M. Sneider, 1992, Geological applications of capillary pressure: A review: AAPG Bulletin, v. 76, p. 840–850.

Walsh, J. B., and W. F. Brace, 1984, The effect of pressure on porosity and the transport properties of rock: Journal of Geophysical Research, v. 89, p. 9425–9431.

Wibberley, C. A. J., G. Yielding, and D.-T. Giulio, 2008, Recent advances in the understanding of fault zone internal structure: A review, *in* C. A. J. Wibberley, W. Kurz, J. Imber, R. E. Holdsworth, and C. Collettini, eds., The internal structure of fault zones: Implications for mechanical and fluid flow properties: Geological Society (London) Special Publication 299, p. 5–33.

Wildenschild, D., R. T. Armstrong, A. L. Herring, I. M. Young, and J. W. Carey, 2011, Exploring capillary trapping efficiency as a function of interfacial tension, viscosity, and flow rate: Energy Procedia, v. 4, p. 4945–4952, doi:10.1016/j.egypro.2011.02.464.

Yielding, G., B. Freemen, and D. T. Needham, 1997, Quantitative fault seal prediction: AAPG Bulletin, v. 81, p. 897–917.